

1 Imaging crossing fibers 2 in mouse, pig, monkey, and human brain 3 using small-angle X-ray scattering

4 Marios Georgiadis^{1,2*}, Miriam Menzel³, Jan A Reuter³, Donald Born⁴, Sophie Kovacevich¹, Dario
5 Alvarez¹, Zirui Gao², Manuel Guizar-Sicairos⁵, Thomas M Weiss⁶, Markus Aixer³, Ivan Rajkovic⁶,
6 Michael M Zeineh¹

7 ¹ Department of Radiology, Stanford School of Medicine, Stanford, CA, USA

8 ² Institute for Biomedical Engineering, ETH Zurich, Zurich, Switzerland

9 ³ Institute of Neuroscience and Medicine (INM-1), Forschungszentrum Jülich GmbH, 52425 Jülich, Germany

10 ⁴ Department of Pathology, Stanford School of Medicine, Stanford, CA, USA

11 ⁵ Photon Science Division, Paul Scherrer Institute, Villigen, Switzerland

12 ⁶ Stanford Synchrotron Radiation Lightsource, SLAC National Accelerator Laboratory, USA

13 *Corresponding Author: Marios Georgiadis, mariosg@stanford.edu

14 Abstract

15 Myelinated axons (nerve fibers) efficiently transmit signals throughout the brain via action
16 potentials. Multiple methods that are sensitive to axon orientations, from microscopy to
17 magnetic resonance imaging, aim to reconstruct the brain's structural connectome. As billions
18 of nerve fibers traverse the brain with various possible geometries at each point, resolving fiber
19 crossings is necessary to generate accurate structural connectivity maps. However, doing so
20 with specificity is a challenging task because signals originating from oriented fibers can be
21 influenced by brain (micro)structures unrelated to myelinated axons.

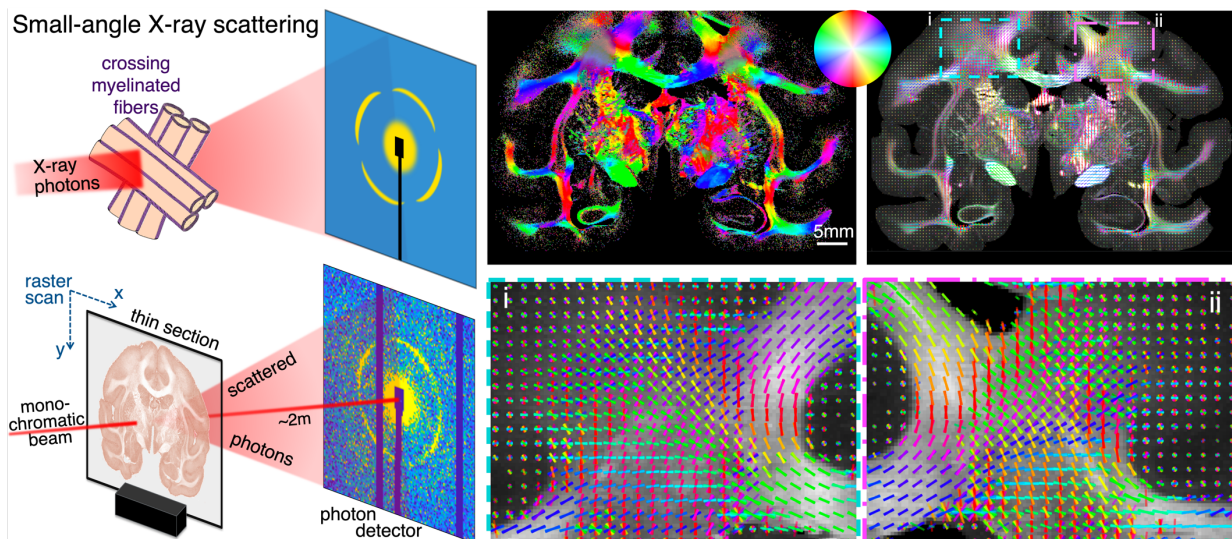
22 X-ray scattering can specifically probe myelinated axons due to the periodicity of the myelin
23 sheath, which yields distinct peaks in the scattering pattern. Here, we show that small-angle X-
24 ray scattering (SAXS) can be used to detect myelinated, axon-specific fiber crossings. We first
25 demonstrate the capability using strips of human corpus callosum to create artificial double-
26 and triple-crossing fiber geometries, and we then apply the method in mouse, pig, vervet
27 monkey, and human brains. Given its specificity, capability of 3-dimensional sampling and high
28 resolution, SAXS can serve as a ground truth for validating MRI as well as microscopy-based
29 methods.

30 **Keywords:** crossing fibers, scanning small-angle X-ray scattering (SAXS), animal and human
31 brain, mouse/pig/vervet monkey brain, human hippocampus, imaging myelinated axons, fiber
32 orientation mapping

33 Statement of Significance

34 To study how the nerve fibers in our brain are interconnected, scientists need to visualize their
35 trajectories, which often cross one another. Here, we show the unique capacity of small-angle
36 X-ray scattering (SAXS) to study these fiber crossings without use of labelling, taking advantage
37 of SAXS's specificity to myelin - the insulating sheath that is wrapped around nerve fibers. We
38 use SAXS to detect double and triple crossing fibers and unveil intricate crossings in mouse, pig,
39 vervet monkey, and human brains. This non-destructive method can uncover complex fiber
40 trajectories and validate other less specific imaging methods (e.g., MRI or microscopy), towards
41 accurate mapping of neuronal connectivity in the animal and human brain.

42 Graphical Abstract



43

44 1 Introduction

45 Signals in the brain are transmitted within neurons via action potentials. These are typically
46 initiated in the soma of neurons, and travel through neuronal axons (nerve fibers) until they
47 reach the synaptic clefts where biochemical mechanisms further transmit the signals to the
48 next cell. A major evolutionary step in the signal transmission in the brain came with
49 myelination: oligodendrocytes, an abundant type of central nervous system glial cells found in
50 vertebrates, form processes that “wrap around” neuronal axons (Schwann cells do the same in
51 the peripheral nervous system). The resulting layered structure around axons is called myelin
52 (with a layer periodicity of ~15-20nm) and is an essential component of our brain, constituting
53 ~35% of its dry weight [1].

54 In the beginning of the 21st century, the “brain connectome” was conceived [2], [3], with
55 the goal of mapping neuronal connections across the animal and human brain. Given that there
56 are >50 billion neurons in a human brain [4], with more than 100,000 km total length of
57 myelinated fibers [5], each of diameter from 0.1 to 100 micrometers [6] (with most axons being
58 around 1µm in diameter), mapping all their connections is an immensely difficult task, for which
59 we currently do not have the imaging tools. However, multiple technologies have been and are
60 being developed to tackle this problem.

61 Neuronal tracers are considered the gold standard for animal neuronal connectivity, as they
62 trace a number of neuronal paths throughout the animal brain [7], [8], with the mouse brain
63 having been studied and mapped extensively [7], [9], [10]. However, the limited ability to study
64 human brains, in addition to the experimental effort for the multiple injections (and animals)
65 and imaging sessions needed to cover a subset of the neurons of a typical animal brain makes
66 this unique method inconvenient for standard assessment of structural connectivity.

67 At the nanometer level, electron microscopy can image at very high resolutions, providing
68 us with exquisite images of human and animal brain at the sub-cellular level, where even single
69 myelin layers can be clearly distinguished [11]. However, electron microscopy typically needs
70 extended sample preparation procedures, which can alter the sample microstructure. Also,
71 even when used in 3D, electron microscopy typically images a small part of the brain at these
72 very high resolutions, usually extending to much less than 1mm³.

73 Alternatively, fluorescence microscopy methods can reach sub-micrometer resolutions, and
74 visualize fibers in extended brain regions [12], while tissue clearing can help image large
75 specimens such as whole mouse or rat brains [13]. However, tissue clearing usually involves
76 tissue distortion and is more difficult for larger and non-perfusion-fixed human tissues.
77 Furthermore, the use of structure tensor analysis, typically accompanying these direct
78 microscopy methods for deriving orientation information, is prone to artifacts due to structures
79 other than axons and can be difficult to apply in dense white matter regions where intensity
80 gradients are small.

81 Imaging methods that directly probe axon orientations overcome many of these issues. 3D
82 Polarized Light Imaging (3D-PLI) exploits the birefringence of myelin to derive fiber orientations
83 in tissue sections at micrometer resolution, with the possible field of view extending to the
84 entire human brain [14]. However, it cannot recover crossing fibers within a pixel, though in-
85 plane pixels are sometimes small enough to still resolve individual bundles crossing one another
86 over several pixels (Zeineh *et al.* [15], Fig 4). Furthermore, the determination of the out-of-
87 plane angle by 3D-PLI is challenging. Polarization-sensitive optical coherence tomography (PS-
88 OCT) in serial, back-scattered mode also provides high-resolution orientation information based

89 on the birefringence of myelin [16], [17] while facilitating image registration, but the method
90 has otherwise similar limitations to 3D-PLI. Scattered light imaging (SLI) [18] partly overcomes
91 those challenges, being able to resolve fiber crossings with micrometer resolution, while also
92 providing information on out-of-plane fiber angles. However, SLI is a new method that still
93 needs validation, especially regarding the quantification of the out-of-plane fiber angles.

94 Finally, the most commonly used method to provide brain-wide structural connectivity is
95 diffusion magnetic resonance imaging (dMRI) [19], [20]. dMRI is sensitive to the anisotropic
96 movement of water molecules, which is used as a proxy for local tissue orientation. However,
97 resolution is typically limited to the hundred micrometers range *ex vivo*, while its signal is also
98 sensitive to tissue microstructures other than myelinated axons, such as non-neuronal cells,
99 extracellular matrix, intracellular components, etc. Most methods used for neuronal orientation
100 analysis to validate dMRI are reviewed in Yendiki *et al.* [21]

101 X-ray scattering probes tissue microstructure by investigating tissue's interactions with X-
102 ray photons traversing the sample: photons elastically deviating from the main path are
103 recorded by an area detector a few meters downstream. When photons probe a highly
104 repetitive structure such as myelin, they constructively interfere at specific angles, forming
105 Bragg peaks (hereafter referred to as "myelin peaks"). Moreover, this constructive interference
106 happens at the plane formed between the photon beam and the direction of periodicity of the
107 repeated structure. In the case of myelin layers, this plane is perpendicular to the nerve fiber
108 orientation. This allows the use of the location of the peaks on the detector for determining the
109 orientation of the myelinated axons (cf. Fig. 1 and Georgiadis *et al.*, 2020 [22]). Use of neutrons
110 instead of photons provides similar information, yet with lower resolution and specificity [23].

111 While determining 3D fiber orientation from scanning **small-angle X-ray scattering** (SAXS)
112 signal has been shown in both thin sections using 3D scanning SAXS [22], [24], [25] and intact
113 tissue specimens using SAXS tensor tomography [26]–[28], the use of scanning SAXS to
114 disentangle crossing fibers in the animal and human brain has not yet been shown. Given the
115 high importance of uncovering interwoven fiber trajectories in connectomics, we sought to
116 determine whether SAXS can delineate crossing fibers. We first demonstrate the use of
117 scanning SAXS to image in-plane crossing fibers in artificial crossings created using strips of
118 human corpus callosum stacked on one another at different angles. In these configurations, we
119 show that SAXS can detect crossing angles down to 25° and distinguish at least 3 crossing fibers.
120 We also demonstrate the detection of crossing fibers in the white and gray matter of brains of
121 multiple species that are actively investigated in connectomics, including mouse, pig, vervet
122 monkey and humans. Taken together, we show scanning SAXS as an imaging tool that is both
123 specific to axonal orientations and sensitive to crossing fiber detection. Scanning SAXS can
124 uncover complex fiber geometries in challenging regions of animal and human brains and
125 therefore serve as validation for state-of-the-art fiber orientation methods such as dMRI or SLI.

126 **2 Methods**

127 **2.1 Brain samples**

128 For creating the artificial crossings of fiber bundles, several sections from a human corpus
129 callosum were used. The brain of a 66-y-o female donor with no sign of neurologic disease was
130 obtained from the Stanford Alzheimer's Disease Research Center Biobank (IRB-approved
131 protocol #33727, including a written informed brain donation consent). It was cut in 1cm
132 coronal slabs, immersion-fixed in 4% paraformaldehyde (PFA) for ~2 weeks, and subsequently
133 stored in a solution of 1x PBS + 0.02% sodium azide to deter bacteria growth. The body of the
134 corpus callosum was excised using a scalpel, and 60 μ m sections were cut using a vibratome
135 (VT1000S, Leica Micro-systems, Germany). The corpus callosum from several consecutive
136 sections was manually cut into small, parallel strips of a few millimeters' width. The tissue strips
137 were manually stacked, aiming to create geometries of two or three fibers crossing, similar to
138 the validation used for SLI [29]. For scanning, the stacked white matter strips were hydrated by
139 phosphate-buffered saline (PBS) and placed between two 150 μ m-thick (#1) cover slips. Cover
140 slips were glued around the edges (Super Glue, The Gorilla Glue Company, USA) to avoid
141 sample dehydration.

142 The mouse brain sections investigated in this study were previously analyzed in [22] to
143 derive single nerve fiber orientations for each tissue pixel. In brief, a vibratome was used to
144 obtain one 25 μ m- and one 50 μ m-thick coronal section from a 5-month-old C57BL/6 female
145 mouse brain, which had previously been fixed by transcardial perfusion with PBS and 4% PFA
146 and then immersed in 4% PFA at 4°C for 48hrs. Procedures were within the animal license
147 ZH242/14 of the Animal Imaging Center of ETH Zurich/University of Zurich. Sections were
148 stored in PBS at 4°C. For scanning, they were enclosed in a PBS bath, within two thin Kapton
149 films (Benetec GmbH, Switzerland) and a custom-made metal frame (see Suppl. Fig. 1 in [22]).

150 The pig brain was extracted from a female 10-week-old micro-Yucatan minipig, following
151 institutional approval. The brain was immersion-fixed in 4% PFA for a month. A coronal slab was
152 cut out of the left hemisphere, and a vibratome (VT1000S, Leica Microsystems, Germany) was
153 used to cut 100- μ m sections. The section together with a minute amount of PBS was placed
154 between #1 cover slips, which were then glued around the edges to avoid sample drying.

155 The vervet monkey brain section was obtained as described in Menzel *et al.* [29] (IACUC
156 #A11-219). Briefly, the extracted brain was fixed in 4% PFA and embedded in a 20% glycerin and
157 2% dimethyl sulfoxide solution before freezing. A cryotome (*Polycut CM 3500*, Leica
158 Microsystems, Germany) was used to obtain 60 μ m-thick sections, stored in 20% glycerin. For
159 the scanning SAXS experiments, one section was immersed in PBS for a few weeks, and then
160 placed between #1 coverslips similar to the pig section and corpus callosum strips.

161 Finally, the human hippocampus section was obtained from the Stanford ADRC Biobank,
162 from the brain of a 80-y-o female donor with a pathologic diagnosis of low Alzheimer's disease
163 (AD staging A1B1C2, Amyloid 1, Braak's 1, Cerad 2, also diagnosed with hippocampal sclerosis
164 of aging, with positive TDP-43 staining). After extraction, the brain was fixed with 4%
165 formaldehyde, cut into 1cm coronal slabs, and stored in PBS. The left hippocampus was excised
166 and a 75 μ m section was obtained using a vibratome (VT1000S, Leica Microsystems, Germany).
167 For scanning, similar to the mouse sections, the human brain section was immersed in PBS and
168 enclosed within two thin Kapton films, surrounded by a metal frame.

169 All animal procedures were in accordance with the National Institutes of Health guidelines
170 for the use and care of laboratory animals and in compliance with the ARRIVE guidelines.

171 2.2 SAXS scanning

172 Each section was raster-scanned by the X-ray beam (details in Table 1). SAXS data were
173 collected by a Pilatus 1M detector (Dectris AG, Switzerland) ~2 meters downstream. A Pilatus
174 2M was used for the mouse data. The beam diameter and motor step sizes were matched (cf
175 Table 1), constituting the effective pixel size for each scan.

176 *Table 1. Experimental details for SAXS scans*

	2x/3x crossings	mouse	pig	vervet	human
Beamline, Synchrotron*	4-2, SSRL	cSAXS, SLS	4-2, SSRL	4-2, SSRL	4-2, SSRL
Container	#1 coverslips	Kapton tapes	#1 coverslips	#1 coverslips	Kapton tapes
Section thickness (μm)	2×60, 3×60	25 50	100	60	75
Beam energy (KeV)	15	12.4 16.3	15	17	11
Beam diameter (μm ²)	125	25 50	100	125	100
Motor step size (μm)	125	25 50	100	125	100
Field of view (x-y matrix)	38 × 39 42 × 46	256 × 400 80 × 102	140 × 199	309 × 480	136 × 250
Exposure time/frame (ms)	500	50 300	500	600	150

177 * SSRL: Stanford Synchrotron Radiation Lightsource, SLS: Swiss Light Source

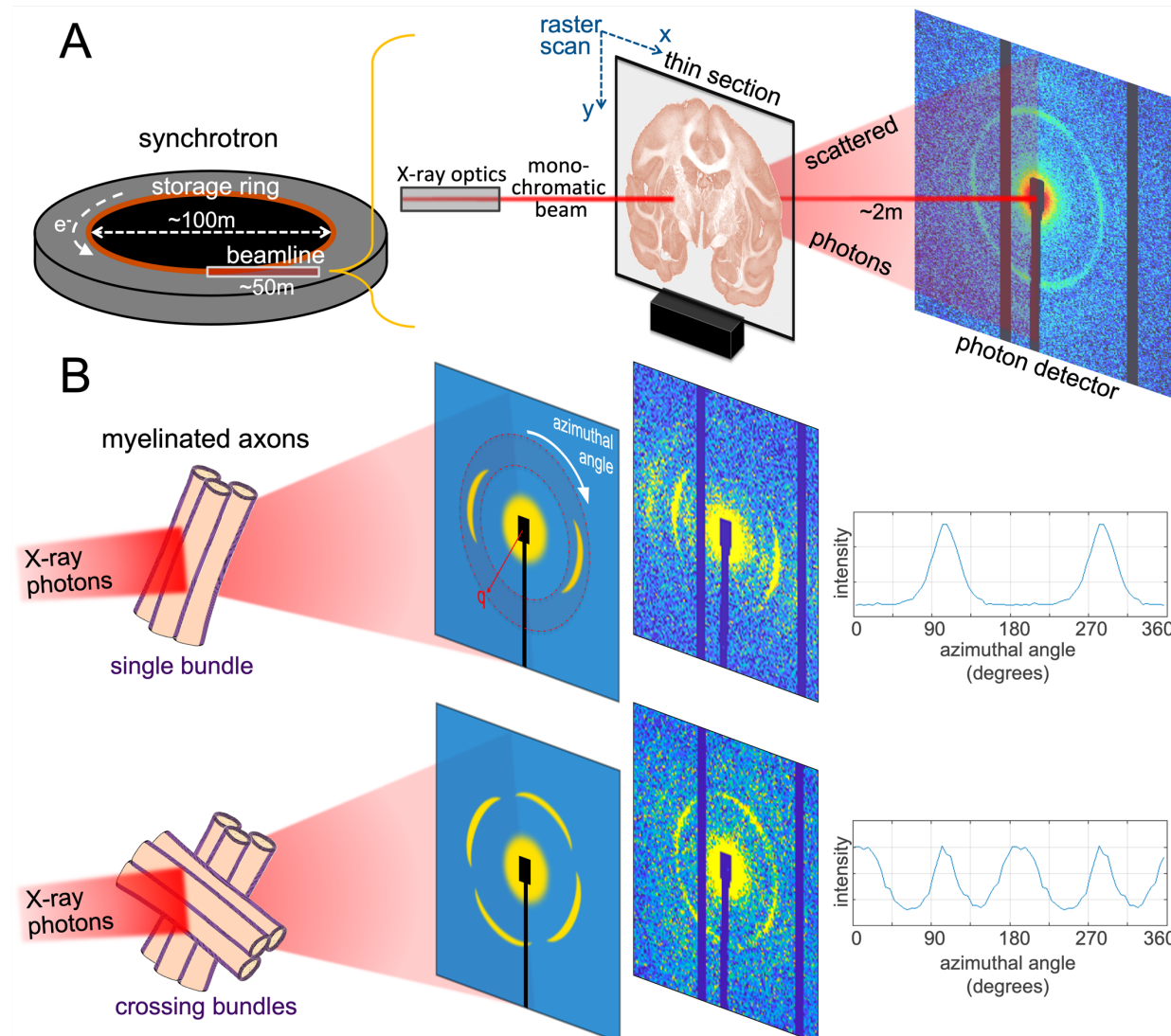
178 2.3 SAXS data analysis

179 A silver behenate (AgBe) standard with known periodicity (5.84nm) was used to identify the
180 scattering pattern center and calibrate the sample-to-detector distance and inverse space units.
181 Each scattering pattern was then segregated into 72 azimuthal segments (5° steps). The signal
182 intensity modulation along the radial direction was obtained for each segment. Photon counts
183 from pixels in 180-degrees opposite segments were averaged due to the center-symmetry of
184 the pattern. This also allows filling in missing information from the regions that correspond to
185 detector electronics (dark bands in scattering patterns, cf. Fig. 1).

186 The myelin-specific signal for each segment was isolated using procedures similar to those
187 described in Georgiadis *et al.* (2021) [28], i.e. by fitting a polynomial to the radial signal intensity
188 curve, and isolating the 2nd order myelin peak (within the red ring in Fig. 1), which is the most
189 prominent peak in myelin scattering patterns [28]. This allowed creating azimuthal profiles for
190 each point, plotted in Fig. 1B, right. These reflect the orientation of the different populations of
191 myelinated fibers within each probed volume (pixel size × section thickness).

192 To quantify and visualize the orientations of crossing nerve fibers, by detecting the peaks
193 and identifying their position, the SLIX software [30] available on <https://github.com/3d-pli/SLIX>
194 was used. This software has been developed to detect up to three different fiber orientations
195 per pixel for scattered light imaging [18], where photons also scatter off the sample depending
196 on nano/microstructure orientation and generate angle-dependent azimuthal profiles and
197 associated peaks [31], a nearly identical computational problem to that with SAXS. Feeding the
198 SAXS azimuthal profile data from each tissue pixel to SLIX produced the single or crossing in-
199 plane fiber orientations per pixel. The SLIX “*--smoothing fourier*” parameters used were
200 0.4/0.225 (default settings suggested by [30]), and 0.1/0.01 for obtaining the main hippocampal
201 fiber orientations (this smoothens the curve only preserving the main peaks). The length of the
202 vectors in vector maps is weighted by the average myelin signal in each pixel.

203 In the orientation encoded colormaps (e.g., in Figs. 2-7A), each pixel is split into 4
204 quadrants, to accommodate 4 possible SLIX-derived fiber orientation colors. If there is a single
205 orientation, all 4 quadrants have the same color. If there are 2 orientations, diagonal quadrants
206 have the same color. If there are 3 orientations, 3 quadrants have corresponding color, and the
207 4th is black.



208
209 **Figure 1.** Detecting myelinated axon orientations using X-ray scattering. A) Schematic of experimental setup in the synchrotron
210 beamline. The monochromatic X-ray beam impinges the thin section and photons are scattered at small angles according to
211 their interactions with the sample's nanostructure and captured by an area detector. B) Principle of detecting (crossing)
212 orientations with sketch (left side) and real data (right side). The X-ray photons interact with the periodic myelin layers (left) and
213 produce peaks in the resulting scattering pattern (middle). The radial position (distance from the pattern center, q) of the peak
214 depends on the myelin layer periodicity d ($q=2\pi/d$), while the azimuthal position depends on the axonal orientations (with
215 photons being scattered at a plane perpendicular to the axon orientation, cf. Georgiadis et al., 2020 [22]). To extract exact
216 axonal orientation, the azimuthal profile of the myelin signal across a ring (in faint red in the top scattering pattern sketch) is
217 plotted (right). The peaks are subsequently identified using the SLIX software (Reuter and Menzel, 2021 [30]). The position of the
218 peaks in the x-axis (which are always 180° apart due to the center-symmetry of the pattern) reflects the fiber orientation angle.
219 In the scattering patterns, the center (where the direct beam lands on the detector) is covered by a beamstop (usually including
220 a photodiode), while the real scattering patterns (right) also have dark stripes (here in the up-down direction) corresponding to
221 detector gaps that accommodate detector electronics. Also, in the real scattering patterns, multiple orders of the myelin peak
222 are visible, albeit at much lower intensities, as expected by the Bragg law combined with the form factor of the myelin layer.

223 2.4 3D-PLI

224 The determination of fiber orientations using 3D-PLI was done in an unstained section of a
225 different C57BL/6 mouse brain. The mouse brain was immersion-fixed in 4% buffered PFA. After
226 cryoprotection (20% glycerol), the brain was deep frozen at -70°C . The brain was serially
227 sectioned along the coronal plane at 60 μm thickness using a cryotome (Leica Microsystems,
228 Germany). Sections were mounted on a glass slide, embedded in 20% glycerol, cover-slipped
229 and sealed with nail polish. The protocol was approved by the institutional animal welfare
230 committee at the Research Centre Jülich, in accordance with European Union (National
231 Institutes of Health) guidelines for the use and care of laboratory animals.

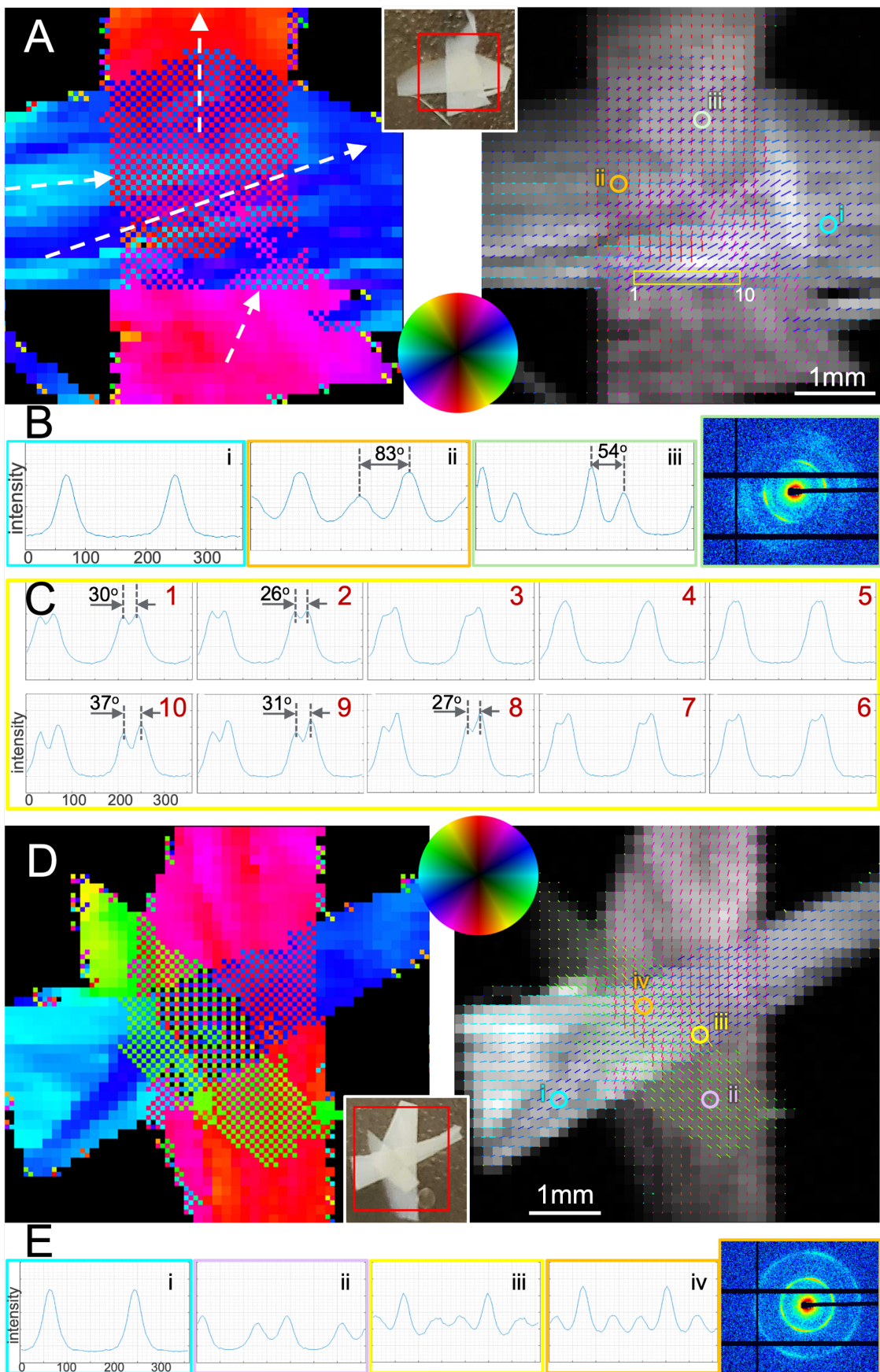
232 Polarimetric measurements of the section were done using the polarizing microscope LMP-
233 1 (Taorad GmbH, Germany). The LMP-1 provides a field of view of $2.7 \times 2.7\text{mm}^2$ and a pixel size
234 of 1.3 μm . Whole mouse brain section scans were carried out tile-wise using a movable
235 specimen stage and a rotating polarizing filter. For each tile, a stack of 18 images was acquired
236 at equidistant rotation angles ($\pm 10^{\circ}$) within the range of 0° to 170° . The measured intensity
237 profile for an individual pixel across the stack of image tiles describes a sinusoidal curve that
238 depends on the spatial orientation of fibers within this pixel. The physical description of the
239 light intensity profile was derived from the Jones calculus for linear optics and represents the
240 basis for orientation analysis, as detailed in [32].

241 3 Results

242 3.1 Validation with artificial crossings - SAXS detects up to three fibers down to 25°
243 crossing angles

244 Analysis of the 2x-fiber configuration (Fig. 2A) shows that SAXS can recover crossing fiber
245 populations. Strong fiber crossings are observed at most pixels in the overlapping region, with
246 varying angles between the fibers in the two tissue strips. In general, the vertical strip shows
247 fibers mostly running up-down (red color), with some rightward orientation of the bottom half
248 (pinkish color). On the other hand, the horizontal strip seems to contain fibers running left-right
249 with an inclination of $\sim 30^{\circ}$ (blue color), e.g., point [i] in right part of Fig. 2A, plotted in Fig. 2B,
250 with some parts having fibers running almost horizontally (cyan). In one such region, at the
251 middle-left of the overlapping region, the fibers seem to cross at almost 90° (Fig. 2A/B, point
252 [ii]). In the upper part of the overlap region, fibers from the two strips seems to cross at angles
253 $\sim 50^{\circ}$ to 60° (cf Fig. 2A/B, point [iii]). While most crossings are resolved, there are small regions
254 (e.g., in the lower and right parts) where the angle between fibers decreases to the point where
255 the two fiber populations are indistinguishable. This resolving limit is shown in the 10 sub-
256 sequent points highlighted with the yellow rectangle in Fig. 2A, of which the azimuthal profiles
257 are displayed in Fig. 2C. Starting from the pixel to the left (#1), the angle between crossing
258 fibers decreases from 30° to 26° (#2), while in pixels #3-7 the two peaks are not distinguished
259 by the algorithm. At pixels #8-10, the two separate fibers are detected again, with angles from
260 27° to 37° respectively.

261 The 3x-fiber configuration (Fig. 2D) showcases the ability of SAXS to detect at least three
262 crossing fiber tracts within a pixel. The fiber orientations from the 3 tissue strips have an
263 average of 60° between them, with the respective peaks clearly distinguishable, Fig. 2E. The
264 majority of pixels in the region of overlap demonstrates 3 orientations, though in some regions
265 only 2 crossing fibers are detected.



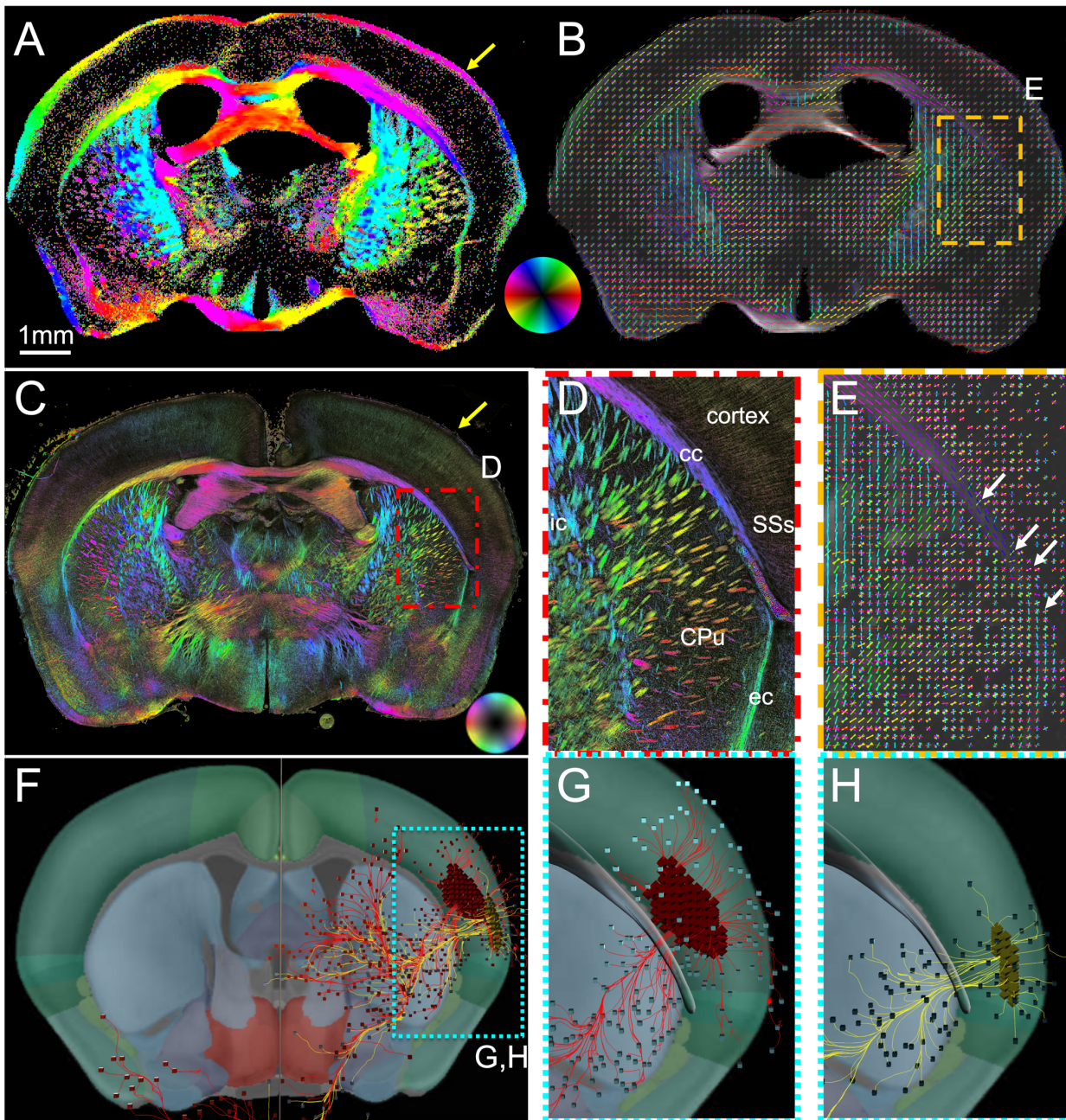
267 **Figure 2.** Imaging fiber orientations in artificial 2x and 3x crossings using strips of human corpus callosum. **A**) Two fiber bundles
268 crossing, with fiber orientations for each pixel encoded in its color (left) or plotted as colored bars (right). Orientation is color-
269 encoded according to the color wheel. Inset: Photo of the fiber strips within the coverslips, with scanned area in red rectangle. **B**)
270 Azimuthal profiles (azimuthal scattering intensity across the myelin peak, cf. Fig. 1) for the circled points in (A). Image outline
271 colors correspond to the colors of the circles in (A). **C**) Azimuthal profiles of 10 subsequent points surrounded by yellow rectangle
272 in (A). Points show transition between two peaks (points 1-2), to one merged peak (points 3-7), and back to two peaks (points 8-
273 10). Limit of detection using SLIX seems to be a crossing angle of approximately 25-30 degrees. **D**) Three fiber bundles crossing,
274 with fiber orientations for each pixel encoded in its color (left) or plotted as colored bars (right). Orientation is color-encoded
275 according to the color wheel. Inset: Photo of the fiber strips within the coverslips, with scanned area in red rectangle. **E**)
276 Azimuthal profiles from select points in (D), with one (cyan), two (magenta), and three (orange & yellow) crossing fibers. As
277 explained in the Methods, in the colored fiber orientation maps (A), (D), each pixel is split into 4 quadrants, to accommodate 4
278 possible SLIX-derived fiber orientation colors. If single orientation, all 4 quadrants have same color. If 2 orientations, diagonal
279 quadrants have same color. If 3 orientation, 3 quadrants have corresponding color, 4th is black.

280 3.2 Mouse brain – detecting fiber crossings in myelinated areas

281 The mouse brain scanning SAXS data analysis using SLIX yielded a detailed fiber orientation
282 map for the 25 μ m-thin section (Fig. 3A,B,E, the latter shows a zoomed-in view of the region of
283 the box from B), revealing intricate crossings in myelinated brain areas. In the white matter,
284 caudoputamen (CPu) fibers merge with the corpus callosum (cc), while some (white arrows)
285 cross the lateral corpus callosum and the external capsule (ec) en route to the cortex,
286 specifically the supplemental somatosensory area (SSs) (anatomic regions delineated on 3D-PLI
287 in D). These crossings can also be inferred from the fiber tract trajectories seen using
288 micrometer-resolution imaging of a section at a ~300 μ m anterior plane from a different mouse
289 with 3D-PLI (Fig. 3C,D, taking into account that 3D-PLI has limited sensitivity to crossing fibers
290 within a pixel). They are more clearly visible in the axons seen by the tracer studies depicted in
291 Fig. 3F-H, from the Allen Mouse Brain Connectivity Atlas [7] (<https://connectivity.brain-map.org/>), corresponding to experiments 297945448-SSs and 520728084-SSs, which include
292 injections in the supplemental somatosensory area. These axons can be clearly seen crossing
293 primarily the lateral side of the corpus callosum and the external capsule to reach the
294 caudoputamen.

295 At the same time, crossings at the edge of the cortex, at the molecular layer, are also visible
296 with scanning SAXS, where myelinated fibers running circumferential to the brain surface to
297 connect to radial fibers from the rest of the cortex (yellow arrow in Fig. 3B), with the
298 circumferentially oriented axons also visible in 3D-PLI (yellow arrow in Fig. 3C).

300 (next page) **Figure 3.** Fiber orientations in the mouse brain using scanning SAXS. **A,B**) Fiber orientations map of 25 μ m-thick
301 section, with orientation color-encoded according to color wheel (A), or with orientation-encoded colored bars (B). To facilitate
302 viewing of the image, one vector for each 5x5 pixel set is shown in (B). **C**) 3D-PLI image showing fiber orientations in a 60 μ m-
303 thick mouse brain section, at a plane ~300 μ m anterior compared to the section in (A-B). **D**) Zoom-in from (C). Yellow arrow
304 points to molecular layer of cortex. **E**) Zoom-in of orange boxed region in (B), where fibers spreading from the internal capsule
305 through the caudoputamen cross the corpus callosum and external capsule (white arrows) to continue radially into the cortex,
306 and radial fibers reach the outermost molecular layer of the cortex and cross with the circumferential myelinated fibers along
307 the brain surface (yellow arrow). **F-H**) Visualization of the Allen Mouse Brain Connectivity Atlas experiments 297945448-SSs and
308 266175461-SSs (<https://connectivity.brain-map.org/projection/experiment/297945448> and <https://connectivity.brain-map.org/projection/experiment/520728084>), which included injections in the supplemental somatosensory area, showing axons
309 in red and yellow colors respectively from a C57BL/6J mouse tagged with green fluorescent protein. **F**) Posterior view of both
310 experiments, with a more anterior coronal section at the back for anatomical reference. **G-H**) Zoom-in from the cyan box in (F),
311 with the corpus callosum in 3D rendering in gray color, rendered semi-transparent to enable visualization of cortical-
312 caudoputamen fibers crossing it. Images created using the Atlas' 3D viewer (<https://connectivity.brain-map.org/3d-viewer>).
313 **cc:** corpus callosum, **ic:** internal capsule, **ec:** external capsule, **CPu:** caudoputamen, **SSs:** supplemental somatosensory area.
314



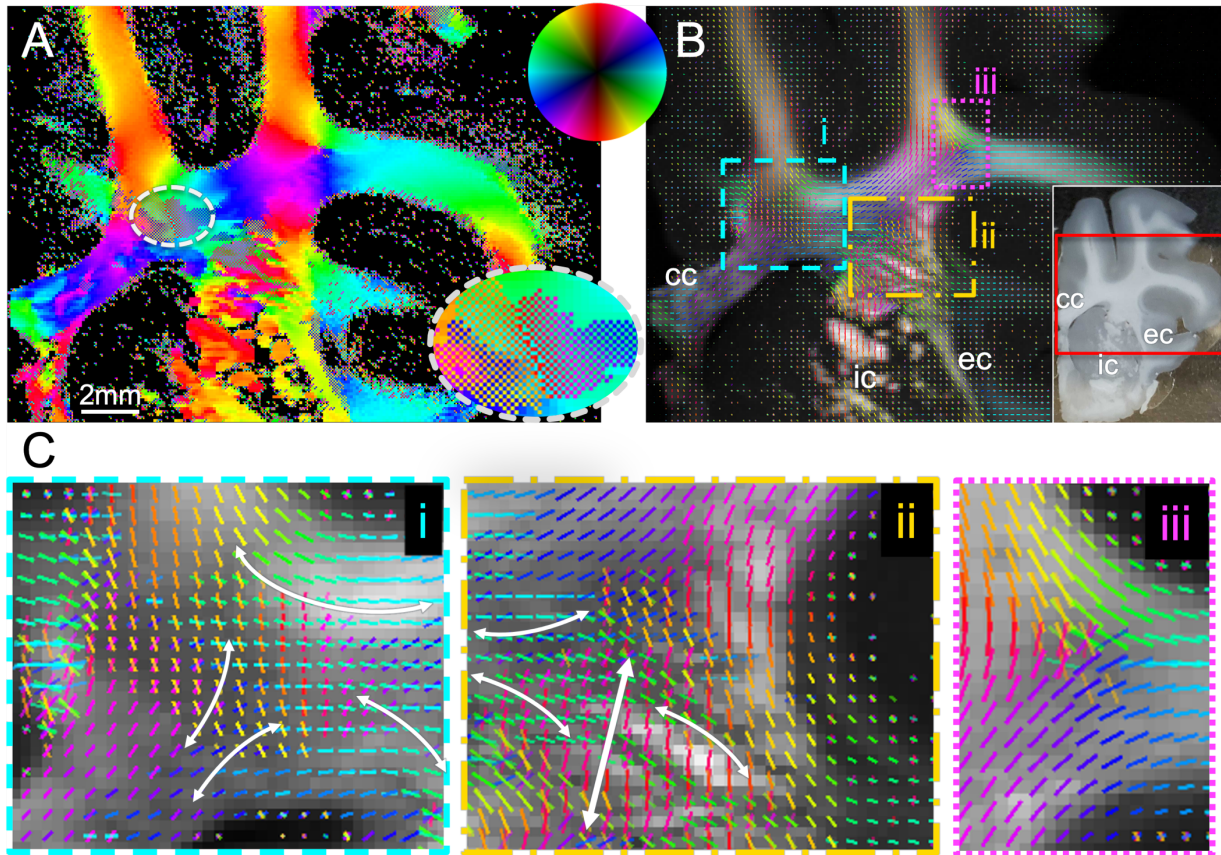
315

316 3.3 Pig brain – imaging complex fiber architectures in white matter

317 Contrary to the commonly studied lissencephalic rodent brain, the pig brain is
318 gyrencephalic, meaning it has a folded structure containing gyri and sulci. This together with its
319 bigger size results in a greater number of myelinated fibers with higher structural complexity of
320 fiber tracts and multiple tract crossings (Fig. 4). The main regions of crossing fibers are enclosed
321 in dotted boxes in Fig. 4B (labelled (i), (ii), and (iii)), and zoomed-in in Fig. 4C. The regions seem
322 to be rich in 2x-fiber crossings, while some triple crossings can also be observed.

323 For instance, region (i) (cyan) contains callosal fibers from the lower left part that curve
324 rightwards or upwards (bottom left pair of white lines), crossing with horizontally-traversing
325 subcortical U-fibers (top arrow) and corticospinal fibers that go to the internal capsule (far-right

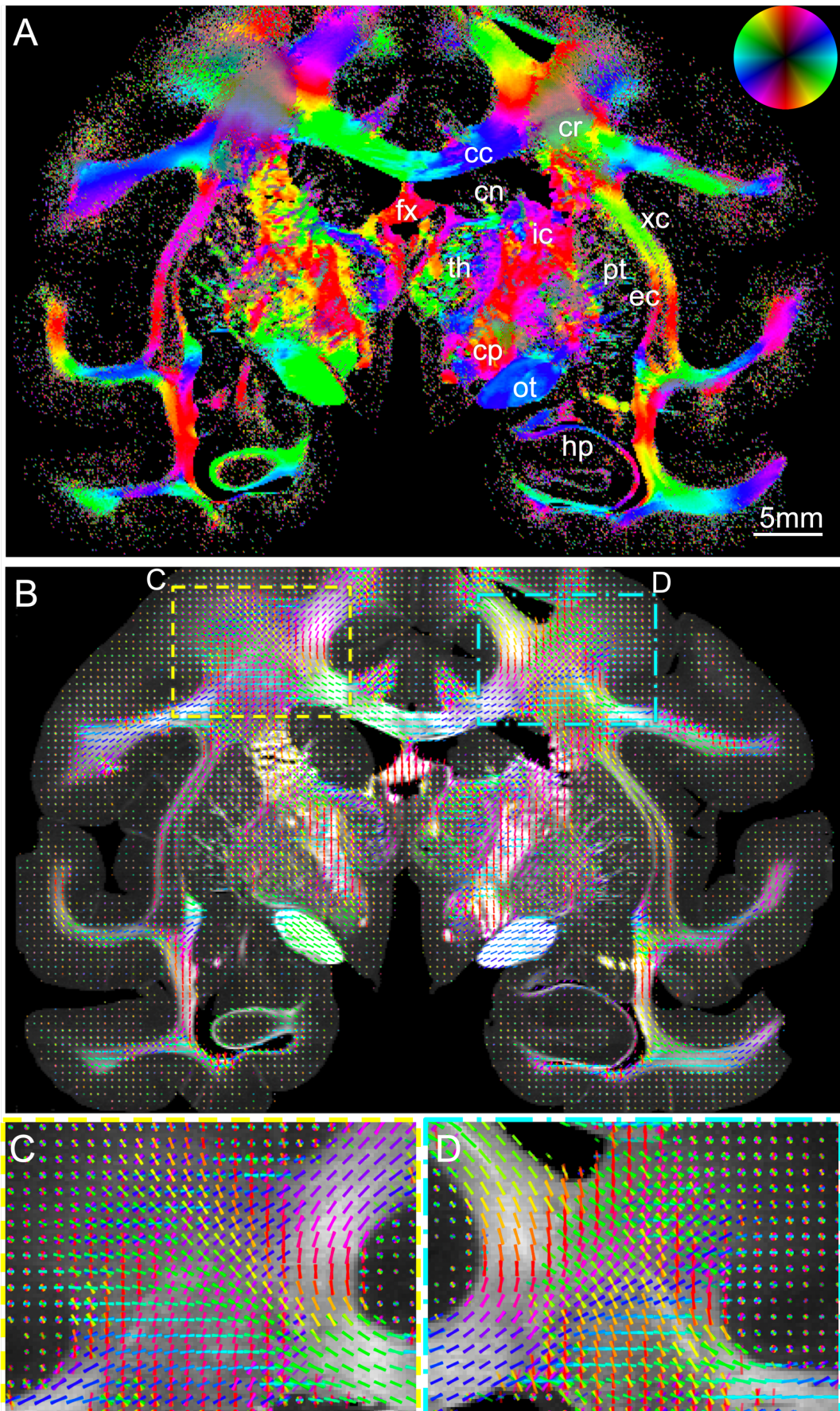
326 arrow). Similarly, in region (ii) (orange), the fibers from the left side (including callosal and
327 subcortical U) or from right side (external capsule) cross with the numerous almost vertical
328 corticospinal fibers from the internal capsule (vertical thick white arrow). Some corticospinal
329 fibers from the superior frontal gyrus (bottom right curved arrow in i) likely join this vertical
330 portion of the internal capsule. Finally, in region (iii) (purple), another subcortical U-fiber
331 population crosses with presumed callosal and internal capsule fibers.



332
333 **Figure 4.** Fiber orientation analysis in the pig coronal section containing part of the corona radiata. A) Fiber orientation map of
334 100μm-thick section, with color encoded fiber orientations according to the color wheel. Inset shows zoomed-in region of
335 crossing fibers, with the colors appearing in a checkerboard pattern, due to multiple orientations per pixel. B) Fiber orientations,
336 represented by orientation-encoded colored bars for each 2x2 pixel set. The inset shows a picture of the pig hemisphere section
337 mounted between the two coverslips, with the red rectangle indicating the region scanned. C) Subregions of the pig section,
338 highlighting areas of various double and triple crossings. cc: corpus callosum, ic: internal capsule, ec: external capsule.

339 3.4 Vervet brain – detecting crossings in challenging primate white matter geometries

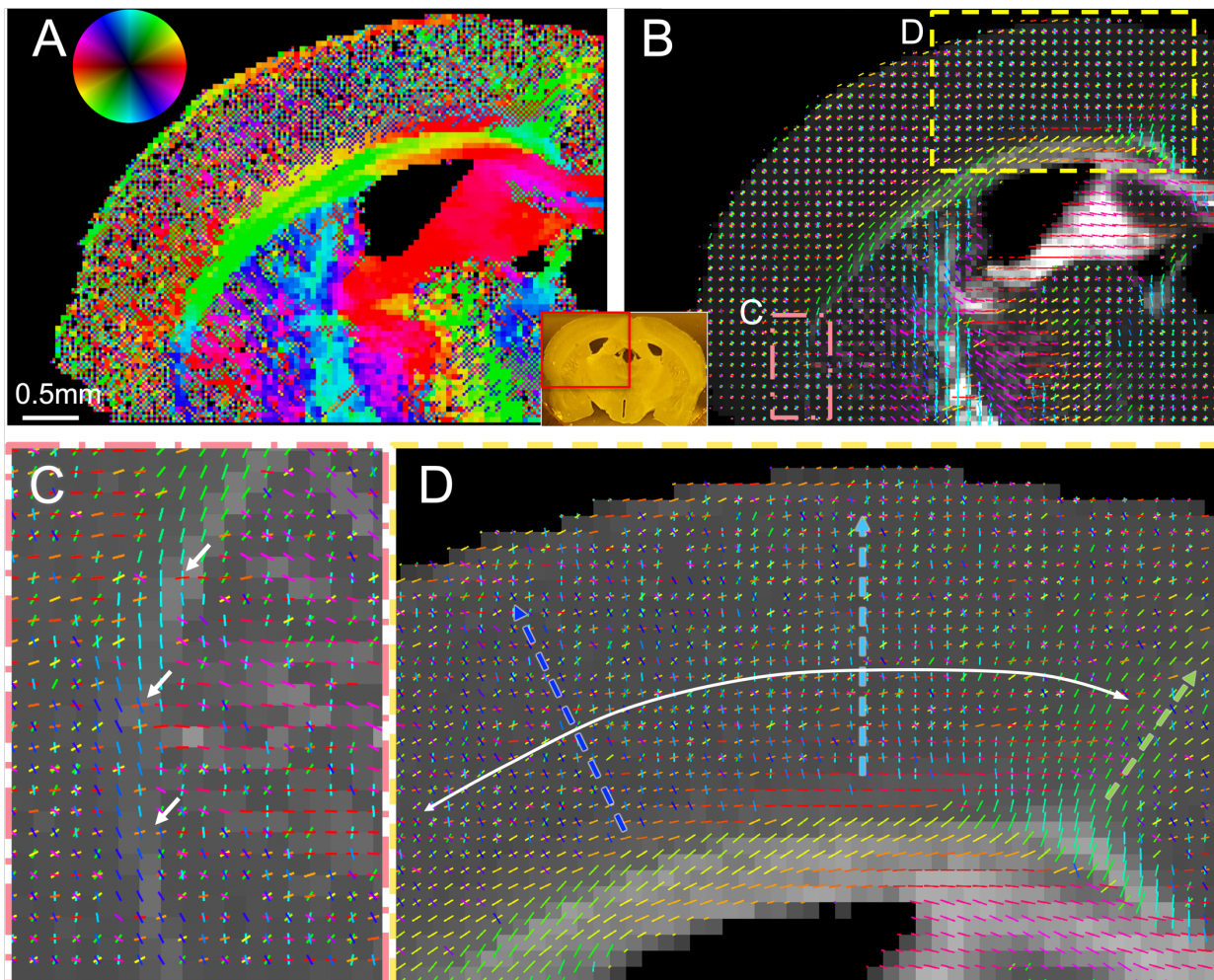
340 The orientation analysis in the vervet brain section produced detailed maps of single and
341 crossing fiber bundles (Fig. 5). Maps of the brain are seen in Figs 5A-B, showing fiber bundles in
342 the corpus callosum (cc), corona radiata (cr), fornix (fx), caudate nucleus (cn), thalamus (th),
343 internal capsule (ic), cerebral peduncle (cp), optic tract (ot), putamen (pt), external capsule (ec),
344 extreme capsule (xc), and hippocampus (hp). The regions with the most prominent crossing
345 fiber populations are those in the corona radiata, Figures 5C and D. There, at least two fiber
346 populations cross, specifically the fibers radiating out of the corpus callosum (mostly left-right
347 direction), and the fibers coming from the internal, external and extreme capsules (mostly
348 superior-inferior direction).



350 **Figure 5.** SAXS fiber orientation analysis in the vervet monkey brain. **A)** Fiber orientation map of 60 μ m-thick section (section nr. 351 518), with fiber orientations color-encoded according to the color wheel. **B)** Fiber orientations for the same section, represented 352 by orientation-encoded colored bars for each 2x2 pixel set. **C-D)** Zoomed-in images of the left and right corona radiata from the 353 vector map. **cc:** corpus callosum, **cr:** corona radiata, **fx:** fornix, **cn:** caudate nucleus, **th:** thalamus, **ic:** internal capsule, **cp:** 354 cerebral peduncle, **ot:** optic tract, **pt:** putamen, **ec:** external capsule, **xc:** extreme capsule, **hp:** hippocampus

355 **3.5 Pushing the limits: imaging gray matter crossings at the mouse cortex**

356 The cortex is known to contain myelinated axons, with complex fiber architecture that can 357 include crossings. Along these lines, apart from the crossings in primarily white matter regions 358 shown in Figure 3 and also depicted here in Fig. 6C, multiple crossings were also detected in 359 gray matter regions of the mouse brain. Figure 6D displays part of the mouse cortex, where 360 myelinated fibers radiate from the corpus callosum towards the periphery in all parts of the 361 cortex. In addition, fibers are observed running through the cortex in a direction tangential to 362 the corpus callosum (e.g. Fig. 6D, in mostly left-right direction, dashed colored arrows show the 363 radial axon orientations, depicted by color-encoded lines).



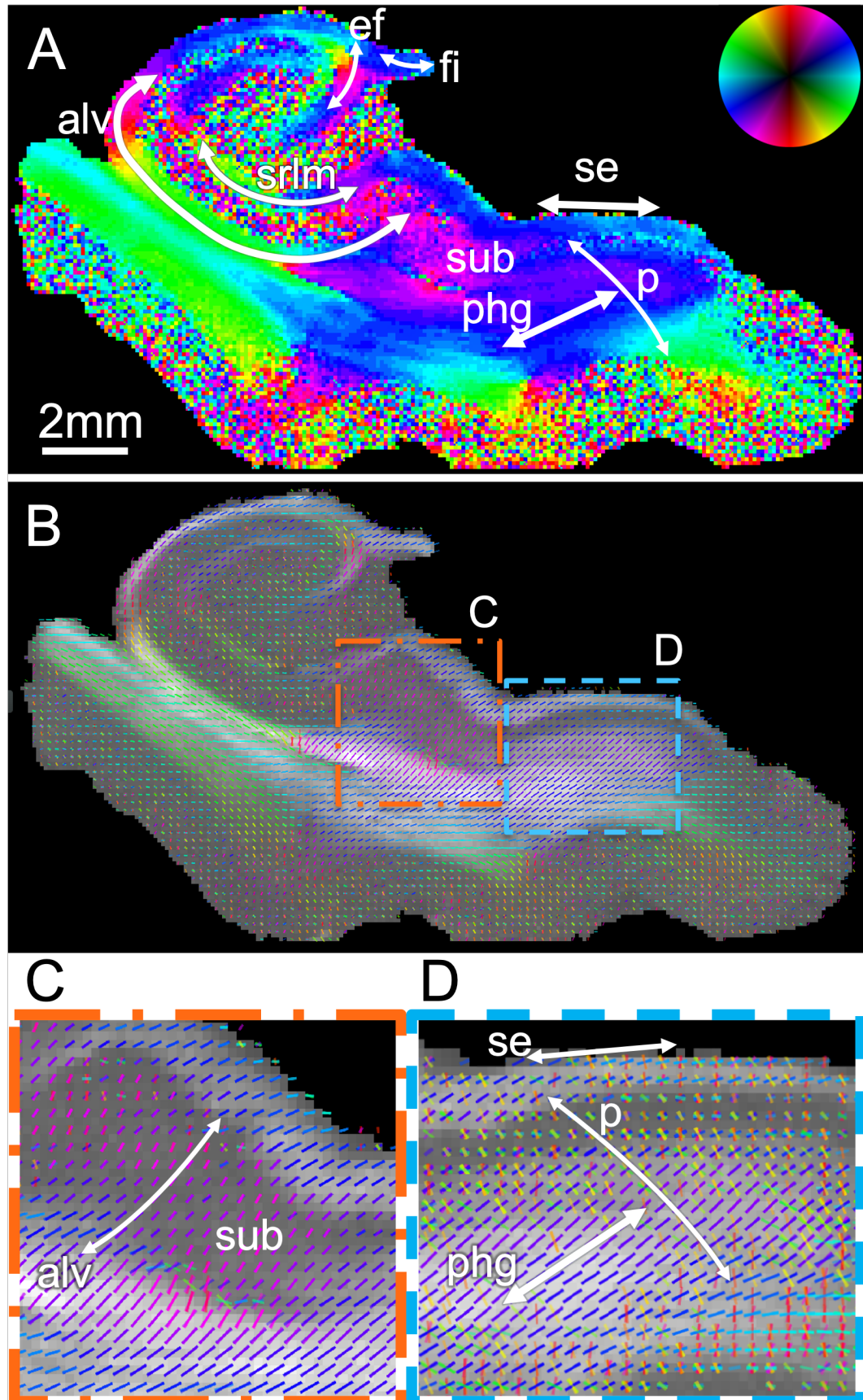
364 **Figure 6.** SAXS of crossing fibers in mouse cortex. **A-B)** Fiber orientation maps of 50 μ m-thick section, located ~200 μ m anterior to 365 section in Fig. 3 (section with scanned region in red rectangle shown in inset). (A) is color-encoded map, (B) is vector map. **C)** 366 Zoom-in of orange-red boxed region in (B), showing white matter fibers radiating from the internal capsule through the 367 caudoputamen and crossing the external capsule fibers (in regions of white arrows) towards the lateral cortex. **D)** Zoom-in of 368 yellow boxed region in (B), including part of the cortex, the corpus callosum and the cingulum. Fibers radiating out of each 369 region of the corpus callosum towards the cortex, are depicted by the blue, cyan and green arrows. Vectors in each pixel in C and 370 D correspond to the nominal image resolution, namely 50 μ m. **371**

372 3.6 Human hippocampus – detecting subtle secondary fiber tract crossings in human
373 brain

374 The human hippocampus is a gray matter structure with numerous interwoven white
375 matter pathways of immense complexity and importance to memory formation, which are
376 altered in neurodegeneration and diseases such as Alzheimer's disease and epilepsy. Analysis of
377 the human hippocampus section provided detailed maps of myelinated axon orientations
378 across hippocampal subfields and the various hippocampal fiber tracts, as demonstrated in
379 Figure 7.

380 Figure 7A shows the color-encoded main fiber orientation for each pixel (achieved by
381 adjusting SLIX parameters to only detect the main peak in the line profiles, cf. Methods),
382 revealing part of the complex anatomy of the hippocampus and the geometry of its fiber
383 bundles. Primary fiber orientations are also depicted visually in Figure 7B, in both white and
384 gray matter areas. The main white matter tracts can be seen there, including the
385 alvear/forniceal (alv), perforant (p), stratum radiatum lacunosum and moleculare (srlm),
386 endfolial (ef) and superficial entorhinal (se) pathways. Subicular fibers heading to/from the
387 alveus (Fig. 7C) are also seen crossing the gray matter. In Figure 7D, the cyan box in (B) is shown
388 in higher resolution, demonstrating secondary and tertiary orientations of myelinated axons
389 within white matter pixels. Multiple fiber orientations can be seen in most white matter pixels,
390 meaning that in the complex hippocampal anatomy and connectivity, each pixel rarely contains
391 fibers from a single bundle. For instance, the perforant pathway (p) is seen crossing the angular
392 bundle within the parahippocampal gyrus (phg) just below the subiculum (sub), and reaching
393 the superficial entorhinal (se) pathway within the stratum radiatum lacunosum and moleculare
394 (srlm) and crossing the subicular forniceal bundle (alv) from 7C.

395 (next page) **Figure 7.** Fiber orientation analysis in the human hippocampus. **A**) Fiber orientation map of a 75 μ m section, with
396 fiber orientations color-encoded according to the color wheel. **B**) Fiber orientations represented by orientation-encoded colored
397 bars for each 2x2 pixel set. Only main orientation is depicted. **C**) Zoomed-in image of the orange box in (B), showing forniceal
398 tract (fo) fibers running through subiculum. **D**) Zoomed-in image of the blue box in (B), depicting both primary and secondary
399 fiber bundles in each pixel. **p**: perforant pathway, **phg**: parahippocampal gyral white matter, **se**: superficial entorhinal pathway,
400 **sub**: subiculum, **fo**: forniceal path, **srlm**: stratum radiatum lacunosum and moleculare, **ef**: endfolial pathway, **fi**: fimbria.



402 4 Discussion

403 In this study, we demonstrate that SAXS can distinguish at least 3 distinct crossing fiber
404 populations, at crossing angles as low as $\sim 25^\circ$, and we show crossings in white and gray matter
405 across different species. This separation is uncovered by analyzing the peaks in the azimuthal
406 profiles from each point's scattering pattern, isolating the myelin signal corresponding to the
407 periodicity of myelin. This work is a critical new direction to scanning SAXS capabilities shown
408 previously, building upon the determination of main 3D fiber orientations in sections [22], [24],
409 comparison to MRI, and quantification of myelin levels, orientation, and integrity in volumetric
410 specimens [28].

411 4.1 Crossing angle detection limit

412 Given the experimental conditions and analysis tools presented in this study, the current
413 limit of detection seems to be approximately 25° - 30° . This resolving power depends on a few
414 factors: first, the signal-to-noise ratio; if less photons impinge the sample, it is possible that
415 noise in the azimuthal profiles could hamper peak detection. However, the current experiments
416 with typical experimental conditions in scanning SAXS seem to yield signals with a high signal-
417 to-noise ratio, which are expected to be robust to such effects. Secondly, there is an inherent
418 resolving limit to the method, which depends on the “fiber response function”, i.e., the angular
419 distribution of the signal coming from a single coherent, unidirectional fiber bundle. In theory,
420 the SAXS signal from a single straight fiber would be exactly at 90 degrees to the fiber
421 orientation and have an azimuthal profile with two peaks of minimal width. However, in
422 practice myelinated axons have some curvature and undulations, and each pixel probed by the
423 beam contains multiple fibers with a certain orientation distribution. Under these
424 circumstances, the effective fiber response function has an azimuthal profile with a distribution
425 similar to the peaks in Figures 1 or 2. Taking these considerations as well as data from the
426 current experiment into account, we speculate that the crossing angle detection could be lower
427 at approximately 20° ; possible improvements to the 25° - 30° presented here could come from
428 higher signal-to-noise ratio experiments (i.e. using higher flux) or even more sensitive peak
429 detection algorithms, as discussed below. Finally, another case where crossing fibers can
430 remain undetected is a scenario where the secondary fiber population contains considerably
431 less myelinated axons (lower number of axons, or axons with a lower degree of myelination). In
432 that case, its scattering peak might not be able to be detected, unless the signal-to-noise ratio is
433 very high or a micrometer-resolution scan can visually resolve the myelinated axons contained
434 in different tracts. Such resolution can be attained by decreasing beam diameter and motor
435 step size, or by use of other orientation-sensitive microscopy methods, such as scattered light
436 imaging [18], [29], [31].

437 4.2 Comparison to other methods

438 Scanning SAXS has different advantages and shortcomings compared to the multiple other
439 methods employed towards detecting fiber orientations -and crossing fibers- in the animal and
440 human brain. Since diffusion MRI is the only modality which can be applied both *in vivo* and *ex*
441 *vivo* with minimal sample preparation, other methods aim to overcome its shortcomings.

442 Limitations of diffusion MRI mostly stem from the fact that it uses the directional
443 movement of water molecules as a proxy for fiber orientation. As a result, i) it is difficult to
444 translate findings from *ex vivo* to *in vivo*, since water content and motility are altered in fixed
445 samples, ii) movement of water is also restricted or hindered by all structures in the brain [33],

446 including membranes of other cells, organelles, extracellular matrix and vesicles, cell
447 cytoskeleton, vesicle walls, while water can passively or actively move across membranes [34],
448 iii) fiber response function is inherently broader compared to SAXS, because even in the case of
449 perfectly aligned fiber population, all the above factors, as well as the movement of water in
450 random directions (to the extent allowed) within the neuronal somata, axons, and in the
451 extracellular space, contribute to an angular dispersion of the signal. In addition, dMRI
452 resolution is typically restricted to hundreds of micrometers per voxel, potentially
453 corresponding to thousands of fibers, further contributing to the angular dispersion. All these
454 make interpretation of diffusion MRI output very challenging and stress the need for validation
455 methods [21].

456 As described, the main limitation of dMRI is lack of specificity to myelinated axons. This can
457 be provided by scanning SAXS, confocal/multi-photon microscopy (possibly combined with
458 clearing), and polarization-based methods (3D-PLI/PS-OCT). The limitation of polarization-based
459 methods is that they are performed on 2D samples (sections or surfaces). On the other hand,
460 confocal/multi-photon microscopy without clearing is limited in depth, and different antibodies
461 can yield different results, depending on the tissue origin, preparation etc., while clearing is
462 labor and time-intensive, typically results in tissue deformation, and is challenging for large
463 specimens. SAXS on the other hand does not depend on staining given its specificity to myelin
464 nanostructure, and X-rays can penetrate thick specimens. Here, we are only reconstructing
465 tissue slices using SAXS. Future implementations of SAXS tensor tomography with crossing fiber
466 detection may provide specificity across a tissue volume.

467 The second feature where dMRI lacks is in resolution, which is limited to hundreds of
468 micrometers. Methods such as 3D-PLI, SLI, and PS-OCT can reach micrometer resolutions, since
469 each image pixel contains orientation information, with SLI also being able to detect crossings
470 in each pixel, while 3D-PLI and PS-OCT depend on their high resolution for visually resolving
471 crossings. Analysis of brightfield or fluorescence images using structure tensor can provide
472 resolution of few to several tens of micrometers, depending on the kernel size used. Electron
473 microscopy is the highest resolution method, reaching sub-nanometer resolutions, but the field
474 of view is typically less than a millimeter, and sample preparation is extensive and usually
475 tissue-distorting. Finally, scanning SAXS orientation analysis can reach sub-micrometer
476 resolutions [35], [36], as it depends on the beamsize and motor step size used, and crossings
477 can be detected for each pixel.

478 Another important advantage of scanning SAXS versus other MRI validation methods is its
479 ability to provide quantitative 3D orientations in isotropic voxels, both tomographically and in
480 sections. Brightfield methods are only 2D, while 3D fluorescence imaging has a lower through-
481 plane compared to in-plane resolution, and structure tensor analysis is challenging in dense
482 white matter regions where intensity gradients are low. 3D-PLI can also provide 3D orientation,
483 but the out-of-plane angle can be ambiguous, while SLI yields information on out-of-plane
484 angles, but quantification has not yet been achieved.

485 Finally, SAXS, in its tensor tomography form [26]–[28], is the only method together with
486 MRI that can be performed on intact specimens, with most other methods being limited to
487 sections. Tissue clearing also enables 3D imaging of specimens, but tissue is usually distorted by
488 the clearing process, and samples larger than few millimeters pose challenges in clearing,
489 antibody penetration and imaging.

490 4.3 Crossings in white and gray matter from multiple species

491 Crossings in the brains of various species are shown in this study. The mouse brain scan
492 revealed crossings in both white and gray matter. White matter crossings were seen mostly by
493 cortical fibers and crossing the corpus callosum and external capsule on their way to the
494 caudoputamen. The relative scarcity of white matter crossings is expected given the rodent
495 brain relative simplicity compared to gyrencephalic brains. Nevertheless, X-ray scattering was
496 also able to distinguish crossings of myelinated axons in gray matter regions, including
497 tangential fibers crossing the more abundant radial ones [37], only previously reported using
498 tracer studies [7], special microscopy methods with very high resolution [38], or diffusion MRI
499 specially utilizing very high angular and spatial resolution [37], [39].

500 Fiber crossings in a Yucatan micropig brain are also reported. Since the pig brain is
501 increasingly used in neuroscientific studies [40], including studies of white matter and structural
502 connectivity [41], [42], it is essential that the white matter fiber orientations are studied and
503 accurately mapped. In addition, the swine model is often used in biomechanical studies [43],
504 where axonal orientation seems to play a role for axonal injury and for computational
505 determination of local mechanical strains [44]. Biomechanical implications of crossing fibers
506 have not been adequately studied to date, so combined imaging and mechanical experiments
507 could help elucidate the structure-biomechanics relationship.

508 The primate (vervet monkey) brain exhibits similar architecture to the human brain, which
509 makes it highly suitable for neuroscientific studies [45] of structure [46] and function [47].
510 Besides, most knowledge of gold-standard human connectivity comes from tracer studies in
511 primates [8], [48], [49]. 3D-PLI of vervet monkey brain regions has provided micrometer
512 resolution fiber orientations maps [46], while SLI has additionally enabled discerning crossing
513 nerve fibers [18], [29], [31]. Our scanning SAXS maps provide detailed fiber crossings across the
514 vervet monkey brain section. The corona radiata SAXS maps appear similar to corona radiata SLI
515 maps [18], [31]. Combining the specificity to myelinated axons of SAXS with the high-resolution
516 capabilities of SLI can potentially help to solve long-standing fiber orientation and tractography
517 issues in brain connectivity, such as the high false-positivity rates of tractography algorithms
518 [50], [51], or the challenges posed in complex fiber geometry regions where multiple fiber
519 bundles combine and have in/through-plane trajectories [51], [52].

520 The human hippocampus is critical for new memory formation, and shows degraded
521 function in neurodegenerative diseases such as Alzheimer's disease (AD) [53]. However, its
522 location towards the lower part of the brain, next to the mastoid air cells, its complex anatomy
523 [54] and connectivity [55] as well as its relatively small size, makes it challenging to study with
524 MRI [56], which is the most commonly used *in vivo* brain imaging modality. Despite that, the
525 significance of the hippocampus has led to multiple approaches to study its detailed anatomy
526 and connectivity. *In vivo* MRI studies have been able to segment the hippocampal subfields
527 [57], and show the main and even microscopic fiber pathways [58], [59]. *Ex vivo*, high-
528 resolution MRI has been commonly used to study hippocampal connectivity in excised
529 specimens; early high-resolution anatomical and diffusion tensor imaging scanning could
530 delineate the different laminae [60], while modern scanners and approaches combining
531 scanning with histology allow detailed subfield segmentation and studies in the context of
532 neurodegenerative diseases [61], [62]. In addition, micrometer-resolution scanning using
533 polarized light imaging has allowed unprecedented insights into the hippocampal connectivity
534 [15]. Here, we have shown myelinated-axon-specific maps of fiber orientations using X-ray

535 scattering in a human hippocampal specimen, including dominant and secondary fiber
536 pathways in white and gray matter. Such information can potentially reveal a loss of normal
537 white matter pathways in neurodegenerative diseases, where demyelination has been
538 observed, as well as loss of specific pathways such as the perforant pathways in AD. This
539 combined with increasing data at the histopathologic [63], cytomic [64], as well as
540 transcriptomic [65], [66] levels can investigate how myelin and oligodendrocytes might be
541 central in the disease mechanisms.

542 **4.4 Limitations**

543 The study has a number of limitations. First, the ground truth for fiber orientations is an
544 ongoing challenge. We attempted to overcome this by i) validating against strips of
545 unidirectional fibers artificially superimposed to mimic pixels with crossings, noting that
546 scanning SAXS has been proven to work in brain tissue for primary orientation [22], [28], and ii)
547 comparing to a micrometer-resolution 3D-PLI image of a similar region of a mouse brain.
548 However, even in the artificial crossings using corpus callosum strips, fibers are not fully aligned
549 within each strip, so ground-truth crossing angles cannot be exactly determined. On the other
550 hand, SAXS yields directional information from myelinated axons directly and with specificity,
551 so the fiber orientations are relatively easily and directly interpreted compared to structural
552 imaging or diffusion MRI, where myelinated-axon-specific orientation analyses include more
553 complex algorithms and more assumptions.

554 SAXS scans can achieve a moderately high resolution while discerning crossing fibers; the
555 highest resolution demonstrated here was in the first mouse brain section, reaching 25
556 micrometers, while resolution was up to 125 micrometers for the vervet brain, much lower
557 than the resolution typically reached in 3D-PLI or SLI. Although SAXS scanning can be performed
558 at very high resolutions, down to nanometer levels [36], practical considerations (beamline
559 capabilities regarding beamsize, and time needed for raster-scanning an extended field of view
560 at such resolutions) limit the resolution to typically tens of micrometers. This is below or at the
561 same order as that of diffusion MRI, with the advantage of specificity to the myelinated fibers,
562 making it thus a very good validation tool for similarly-sized samples.

563 Sensitivity to peak detection in the azimuthal profiles presents a challenge for future
564 improvements. In this study, the SLIX software [30] used the SAXS azimuthal profile data as
565 input, since in SLI photons also scatter anisotropically off material depending on structure
566 orientation, and in both methods the position of the peaks in azimuthal profiles reveals the in-
567 plane orientation of the fibers. However, by looking at the azimuthal profiles of pixels 3, 6, and
568 7 in Fig. 2, one can suggest that there are two peaks that are at an angle of $\sim 20^\circ$ apart. This
569 could indicate that a more sensitive peak-fitting algorithm, the subject of our future work, could
570 possibly be able to tell these peaks apart, and thus resolve even lower angle crossings.

571 When it comes to tissue preparation for imaging, the presented scanning SAXS experiments
572 were performed on thin sections. Although this is a very common approach used in histology or
573 methods such as 3D-PLI or SLI, in many cases it is not desired, or not feasible. However, with
574 the advent of SAXS tensor tomography [26], [28], such experiments can also be performed
575 tomographically on whole specimens without sectioning. The challenge of computing both the
576 tensor-tomographic reconstruction and depicting multiple fiber orientations per voxel will also
577 be the subject of future investigations. This would provide a tomographic gold-standard in the
578 axonal orientation field and enable a head-to-head validation of diffusion MRI orientation
579 information on the same specimens.

580 Access to scanning SAXS is also a limitation because the required photon flux of micro-
581 focused beam is currently only obtainable from synchrotrons. However, several sites worldwide
582 provide appropriate beamlines for collaborative use. Continued improvement of
583 instrumentation and analysis will enable higher sample throughput as well as scanning SAXS
584 experiments on lab SAXS setups.

585 5 Conclusion

586 Accurate and specific imaging of crossing nerve fibers is an important challenge in
587 neuroscience. In the experiments presented here, we use scanning small-angle X-ray scattering
588 (SAXS) to show that detecting crossing fibers is feasible for at least three crossing fiber bundles
589 and crossing angles down to approximately 25°, and applied the method across species, in
590 mouse, pig, vervet monkey, and human brain, in gray and white matter. Overall, as scanning
591 SAXS can provide specificity to myelinated axonal orientations, which are responsible for long-
592 distance signal transmission in the brain, it has the potential to become a reference method for
593 accurate fiber orientation mapping. Combination of scanning SAXS with micrometer-resolution
594 imaging approaches, such as 3D-PLI or SLI, taking advantage of SAXS's specificity and 3D-PLI/SLI
595 resolution, could provide ground truth information on fiber orientations, yield accurate
596 structural connectivity maps and be the basis for validation of diffusion MRI signals.

597 Acknowledgments

598 We thank Samuel Baker from Stanford Comparative Medicine, Aileen Schroeter and Markus
599 Rudin from ETH Zurich, Roger Woods from the UCLA Brain Research Institute and Donald Born
600 from Stanford Neuropathology for providing the pig, mouse, vervet and human brain samples
601 respectively, as well as all animal and human donors. The present work was supported by the
602 National Institutes of Health (NIH), award numbers R01NS088040, P41EB017183,
603 R01AG061120-01, R01MH092311, and 5P40OD010965, and by the European Union's Horizon
604 2020 Research and Innovation Programme under Grant Agreement No. 945539 ("Human Brain
605 Project" SGA3). 3D-PLI images were generated by utilizing the computing time granted through
606 JARA-HPC on the supercomputer JURECA at Forschungszentrum Juelich (FZJ), Germany. SSRL,
607 SLAC National Accelerator Laboratory, is supported by the U.S. Department of Energy, under
608 Contract No. DE-AC02-76SF00515. The SSRL Structural Molecular Biology Program is supported
609 by the DOE Office of Biological and Environmental Research, and by the National Institutes of
610 Health, National Institute of General Medical Sciences (P30GM133894). The Pilatus detector at
611 beamline 4-2 at SSRL was funded under National Institutes of Health Grant S10OD021512. The
612 experiment on mouse brain sections were carried out at the cSAXS beamline, Swiss Light
613 Source, Paul Scherrer institute, Switzerland, and the artificial crossings, pig, vervet and human
614 sections in the 4-2 beamline of Stanford Synchrotron Radiation Lightsource, SLAC National La-
615 boration, USA.

616 Data statement

617 SAXS data for all samples are deposited at: <https://doi.org/10.5281/zenodo.7228131>

618 The authors declare no competing interest.

619 **References**

620 [1] P. Morell, *Myelin*, 2nd ed. New York: Springer Science+Business Media, 1984.

621 [2] O. Sporns, G. Tononi, and R. Kötter, "The human connectome: a structural description of
622 the human brain," *PLoS Comput Biol*, vol. 1, no. 4, p. e42, 2005.

623 [3] P. Hagmann, "From diffusion MRI to brain connectomics," EPFL, 2005.

624 [4] F. A. C. Azevedo *et al.*, "Equal numbers of neuronal and nonneuronal cells make the
625 human brain an isometrically scaled-up primate brain," *J. Comp. Neurol.*, vol. 513, no. 5,
626 pp. 532–541, 2009.

627 [5] Y. Tang and J. R. Nyengaard, "A stereological method for estimating the total length and
628 size of myelin fibers in human brain white matter," *J. Neurosci. Methods*, vol. 73, no. 2,
629 pp. 193–200, 1997.

630 [6] A. Peters, S. L. Palay, and H. deF. Webster, *The Fine Structure of the Nervous System.
631 Neurons and their Supporting Cells*, 3rd ed. New York: Oxford University Press, 1991.

632 [7] S. W. Oh *et al.*, "A mesoscale connectome of the mouse brain," *Nature*, vol. 508, p. 207,
633 2014.

634 [8] N. T. Markov *et al.*, "A weighted and directed interareal connectivity matrix for macaque
635 cerebral cortex," *Cereb. Cortex*, vol. 24, no. 1, pp. 17–36, Jan. 2014.

636 [9] J. A. Harris *et al.*, "Hierarchical organization of cortical and thalamic connectivity,"
637 *Nature*, vol. 575, no. 7781, pp. 195–202, 2019.

638 [10] H. Hintiryan *et al.*, "The mouse cortico-striatal projectome," *Nat. Neurosci.*, vol. 19, no. 8,
639 pp. 1100–1114, 2016.

640 [11] W. Möbius, K.-A. Nave, and H. B. Werner, "Electron microscopy of myelin: Structure
641 preservation by high-pressure freezing," *Brain Res.*, vol. 1641, pp. 92–100, 2016.

642 [12] L. J. Hogstrom, S. M. Guo, K. Murugadoss, and M. Bathe, "Advancing multiscale structural
643 mapping of the brain through fluorescence imaging and analysis across length scales,"
644 *Interface Focus*, vol. 6, no. 1, p. 20150081, Feb. 2016.

645 [13] K. Chung and K. Deisseroth, "CLARITY for mapping the nervous system," *Nat Meth*, vol.
646 10, no. 6, pp. 508–513, 2013.

647 [14] M. Axer *et al.*, "A novel approach to the human connectome: Ultra-high resolution
648 mapping of fiber tracts in the brain," *Neuroimage*, vol. 54, no. 2, pp. 1091–1101, 2011.

649 [15] M. M. Zeineh *et al.*, "Direct Visualization and Mapping of the Spatial Course of Fiber
650 Tracts at Microscopic Resolution in the Human Hippocampus," *Cereb Cortex*, vol. 27, no.
651 3, pp. 1779–1794, 2017.

652 [16] H. Wang *et al.*, "Cross-validation of serial optical coherence scanning and diffusion tensor
653 imaging: A study on neural fiber maps in human medulla oblongata," *Neuroimage*, vol.
654 100, pp. 395–404, 2014.

655 [17] R. Jones *et al.*, "Insight into the fundamental trade-offs of diffusion MRI from
656 polarization-sensitive optical coherence tomography in ex vivo human brain,"
657 *Neuroimage*, vol. 214, p. 116704, 2020.

658 [18] M. Menzel *et al.*, "Scattered Light Imaging: Resolving the substructure of nerve fiber
659 crossings in whole brain sections with micrometer resolution," *Neuroimage*, vol. 233, p.
660 117952, 2021.

661 [19] H. Johansen-Berg and M. F. Rushworth, "Using diffusion imaging to study human
662 connectional anatomy," *Annu Rev Neurosci*, vol. 32, pp. 75–94, 2009.

663 [20] B. J. Jellison, A. S. Field, J. Medow, M. Lazar, M. S. Salamat, and A. L. Alexander,

664 "Diffusion tensor imaging of cerebral white matter: A pictorial review of physics, fiber
665 tract anatomy, and tumor imaging patterns," *Am. J. Neuroradiol.*, vol. 25, no. 3, pp. 356–
666 369, 2004.

667 [21] A. Yendiki, M. Aggarwal, M. Aixer, A. F. D. Howard, A.-M. van C. van Walsum, and S. N.
668 Haber, "Post mortem mapping of connectional anatomy for the validation of diffusion
669 MRI," *Neuroimage*, vol. 256, p. 119146, 2022.

670 [22] M. Georgiadis *et al.*, "Retrieving neuronal orientations using 3D scanning SAXS and
671 comparison with diffusion MRI," *Neuroimage*, vol. 204, p. 116214, 2020.

672 [23] S. Maiti, H. Frielinghaus, D. Gräßel, M. Dulle, M. Aixer, and S. Förster, "Distribution and
673 orientation of nerve fibers and myelin assembly in a brain section retrieved by small-
674 angle neutron scattering," *Sci. Rep.*, vol. 11, no. 1, p. 17306, 2021.

675 [24] M. Georgiadis *et al.*, "3D scanning SAXS: A novel method for the assessment of bone
676 ultrastructure orientation," *Bone*, vol. 71, no. 0, pp. 42–52, 2015.

677 [25] M. Georgiadis *et al.*, "Ultrastructure organization of human trabeculae assessed by 3D
678 sSAXS and relation to bone microarchitecture," *PLoS One*, vol. 11, no. 8, p. e0159838,
679 2016.

680 [26] M. Liebi *et al.*, "Nanostructure surveys of macroscopic specimens by small-angle
681 scattering tensor tomography," *Nature*, vol. 527, no. 7578, pp. 349–352, 2015.

682 [27] M. Liebi *et al.*, "Small-angle X-ray scattering tensor tomography: model of the three-
683 dimensional reciprocal-space map, reconstruction algorithm and angular sampling
684 requirements," *Acta Crystallogr A Found Adv*, vol. 74, no. Pt 1, pp. 12–24, 2018.

685 [28] M. Georgiadis *et al.*, "Nanostructure-specific X-ray tomography reveals myelin levels,
686 integrity and axon orientations in mouse and human nervous tissue," *Nat. Commun.*, vol.
687 12, no. 2941, 2021.

688 [29] M. Menzel *et al.*, "Toward a High-Resolution Reconstruction of 3D Nerve Fiber
689 Architectures and Crossings in the Brain Using Light Scattering Measurements and Finite-
690 Difference Time-Domain Simulations," *Phys. Rev. X*, vol. 10, no. 2, p. 21002, Apr. 2020.

691 [30] J. A. Reuter and M. Menzel, "SLIX: A Python package for fully automated evaluation of
692 Scattered Light Imaging measurements on brain tissue," *J. Open Source Softw.*, vol. 5, no.
693 54, p. 2675, 2020.

694 [31] M. Menzel, M. Ritzkowski, J. A. Reuter, D. Gräßel, K. Amunts, and M. Aixer,
695 "Scatterometry Measurements With Scattered Light Imaging Enable New Insights Into
696 the Nerve Fiber Architecture of the Brain ,," *Frontiers in Neuroanatomy* , vol. 15. 2021.

697 [32] M. Stacho *et al.*, "A cortex-like canonical circuit in the avian forebrain," *Science (80-.)*,
698 vol. 369, no. 6511, p. eabc5534, Sep. 2020.

699 [33] C. Beaulieu, "The basis of anisotropic water diffusion in the nervous system—a technical
700 review," *NMR Biomed.*, vol. 15, no. 7-8, pp. 435–455, 2002.

701 [34] N. MacAulay, "Molecular mechanisms of brain water transport," *Nat. Rev. Neurosci.*, vol.
702 22, no. 6, pp. 326–344, 2021.

703 [35] H. Inouye *et al.*, "Myelin organization in the nodal, paranodal, and juxtaparanodal
704 regions revealed by scanning x-ray microdiffraction," *PLoS One*, vol. 9, no. 7, p. e100592,
705 2014.

706 [36] H. Inouye, F.-H. Kuo, A. R. Denninger, B. Weinhausen, M. Burghammer, and D. A.
707 Kirschner, "Myelin structure in unfixed, single nerve fibers: Scanning X-ray
708 microdiffraction with a beam size of 200nm," *J. Struct. Biol.*, 2017.

709 [37] O. F. Gulban, F. De Martino, A. T. Vu, E. Yacoub, K. Uğurbil, and C. Lenglet, "Cortical fibers
710 orientation mapping using in-vivo whole brain 7 T diffusion MRI," *Neuroimage*, vol. 178,
711 pp. 104–118, Sep. 2018.

712 [38] M. J. Redlich and H. Lim, "A Method to Measure Myeloarchitecture of the Murine
713 Cerebral Cortex in vivo and ex vivo by Intrinsic Third-Harmonic Generation," *Front.
714 Neuroanat.*, vol. 13, p. 65, Jun. 2019.

715 [39] C. W. U. Leuze *et al.*, "Layer-specific intracortical connectivity revealed with diffusion
716 MRI," *Cereb. Cortex*, vol. 24, no. 2, pp. 328–339, Feb. 2014.

717 [40] N. M. Lind, A. Moustgaard, J. Jelsing, G. Vajta, P. Cumming, and A. K. Hansen, "The use of
718 pigs in neuroscience: Modeling brain disorders," *Neurosci. Biobehav. Rev.*, vol. 31, no. 5,
719 pp. 728–751, 2007.

720 [41] R. A. Benn *et al.*, "Opening the Pig to Comparative Neuroimaging: A Common Space
721 Approach Contextualizes the Pig and Human Structural Connectome," *bioRxiv*, p.
722 2020.10.13.337436, Jan. 2022.

723 [42] M. C. Ryan *et al.*, "Miniature pig model of human adolescent brain white matter
724 development," *J. Neurosci. Methods*, vol. 296, pp. 99–108, 2018.

725 [43] H. A. Kinder, E. W. Baker, and F. D. West, "The pig as a preclinical traumatic brain injury
726 model: current models, functional outcome measures, and translational detection
727 strategies," *Neural Regen. Res.*, vol. 14, no. 3, pp. 413–424, Mar. 2019.

728 [44] Z. Zhou *et al.*, "White Matter Tract-Oriented Deformation Is Dependent on Real-Time
729 Axonal Fiber Orientation," *J. Neurotrauma*, vol. 38, no. 12, pp. 1730–1745, Jan. 2021.

730 [45] A. J. Jasinska *et al.*, "Systems Biology of the Vervet Monkey," *ILAR J.*, vol. 54, no. 2, pp.
731 122–143, Jan. 2013.

732 [46] H. Takemura *et al.*, "Anatomy of nerve fiber bundles at micrometer-resolution in the
733 vervet monkey visual system," *Elife*, vol. 9, p. e55444, 2020.

734 [47] R. Gil-da-Costa and M. D. Hauser, "Vervet monkeys and humans show brain asymmetries
735 for processing conspecific vocalizations, but with opposite patterns of laterality," *Proc. R.
736 Soc. B Biol. Sci.*, vol. 273, no. 1599, pp. 2313–2318, Sep. 2006.

737 [48] M. Yan *et al.*, "Mapping brain-wide excitatory projectome of primate prefrontal cortex at
738 submicron resolution and comparison with diffusion tractography," *Elife*, vol. 11, p.
739 e72534, 2022.

740 [49] F. Xu *et al.*, "High-throughput mapping of a whole rhesus monkey brain at micrometer
741 resolution," *Nat. Biotechnol.*, vol. 39, no. 12, pp. 1521–1528, 2021.

742 [50] S. Simona *et al.*, "A new method for accurate in vivo mapping of human brain
743 connections using microstructural and anatomical information," *Sci. Adv.*, vol. 6, no. 31,
744 p. eaba8245, Jun. 2022.

745 [51] K. H. Maier-Hein *et al.*, "The challenge of mapping the human connectome based on
746 diffusion tractography," *Nat. Commun.*, vol. 8, no. 1, p. 1349, 2017.

747 [52] C. Maffei *et al.*, "Insights from the IronTract challenge: Optimal methods for mapping
748 brain pathways from multi-shell diffusion MRI," *Neuroimage*, vol. 257, p. 119327, 2022.

749 [53] K. S. Anand and V. Dhikav, "Hippocampus in health and disease: An overview," *Ann.
750 Indian Acad. Neurol.*, vol. 15, no. 4, pp. 239–246, Oct. 2012.

751 [54] H. Duvernoy, F. Cattin, and P.-Y. Risold, "Anatomy BT - The Human Hippocampus:
752 Functional Anatomy, Vascularization and Serial Sections with MRI," H. M. Duvernoy, F.
753 Cattin, and P.-Y. Risold, Eds. Berlin, Heidelberg: Springer Berlin Heidelberg, 2013, pp. 39–

754 68.

755 [55] H. Duvernoy, F. Cattin, and P.-Y. Risold, "Structure, Functions, and Connections BT - The
756 Human Hippocampus: Functional Anatomy, Vascularization and Serial Sections with
757 MRI," H. M. Duvernoy, F. Cattin, and P.-Y. Risold, Eds. Berlin, Heidelberg: Springer Berlin
758 Heidelberg, 2013, pp. 5–38.

759 [56] H. Duvernoy, F. Cattin, and P.-Y. Risold, "Sectional Anatomy and Magnetic Resonance
760 Imaging BT - The Human Hippocampus: Functional Anatomy, Vascularization and Serial
761 Sections with MRI," H. M. Duvernoy, F. Cattin, and P.-Y. Risold, Eds. Berlin, Heidelberg:
762 Springer Berlin Heidelberg, 2013, pp. 127–213.

763 [57] A. D. Ekstrom *et al.*, "Advances in high-resolution imaging and computational unfolding
764 of the human hippocampus," *Neuroimage*, vol. 47, no. 1, pp. 42–49, 2009.

765 [58] M. B. Parekh, B. K. Rutt, R. Purcell, Y. Chen, and M. M. Zeineh, "Ultra-high resolution in-
766 vivo 7.0T structural imaging of the human hippocampus reveals the endfolial pathway,"
767 *Neuroimage*, vol. 112, pp. 1–6, 2015.

768 [59] M. M. Zeineh, S. Holdsworth, S. Skare, S. W. Atlas, and R. Bammer, "Ultra-high resolution
769 diffusion tensor imaging of the microscopic pathways of the medial temporal lobe.,"
770 *Neuroimage*, vol. 62, no. 3, pp. 2065–2082, Sep. 2012.

771 [60] T. M. Shepherd, E. Özarslan, A. T. Yachnis, M. A. King, and S. J. Blackband, "Diffusion
772 Tensor Microscopy Indicates the Cytoarchitectural Basis for Diffusion Anisotropy in the
773 Human Hippocampus," *Am. J. Neuroradiol.*, vol. 28, no. 5, pp. 958 LP – 964, May 2007.

774 [61] A. D. H. *et al.*, "Characterizing the human hippocampus in aging and Alzheimer's disease
775 using a computational atlas derived from ex vivo MRI and histology," *Proc. Natl. Acad.
776 Sci.*, vol. 115, no. 16, pp. 4252–4257, Apr. 2018.

777 [62] S. Ravikumar *et al.*, "Ex vivo MRI atlas of the human medial temporal lobe: characterizing
778 neurodegeneration due to tau pathology," *Acta Neuropathol. Commun.*, vol. 9, no. 1, p.
779 173, 2021.

780 [63] K.-H. Tse, A. Cheng, F. Ma, and K. Herrup, "DNA damage-associated oligodendrocyte
781 degeneration precedes amyloid pathology and contributes to Alzheimer's disease and
782 dementia," *Alzheimer's Dement.*, vol. 14, no. 5, pp. 664–679, 2018.

783 [64] S. Safaiyan *et al.*, "Age-related myelin degradation burdens the clearance function of
784 microglia during aging," *Nat. Neurosci.*, vol. 19, no. 8, pp. 995–998, 2016.

785 [65] T. Iram *et al.*, "Young CSF restores oligodendrogenesis and memory in aged mice via
786 Fgf17," *Nature*, vol. 605, no. 7910, pp. 509–515, 2022.

787 [66] H. Mathys *et al.*, "Single-cell transcriptomic analysis of Alzheimer's disease," *Nature*, vol.
788 570, no. 7761, pp. 332–337, 2019.